A non-isothermal phase-field crystal model with lattice expansion: analysis and benchmarks

To cite this article: Maik Punke *et al* 2025 *Modelling Simul. Mater. Sci. Eng.* **33** 025007

OPEN ACCESS
IOP Publishing
Modelling and Simulation in Materials Science and Engineering

Modelling Simul. Mater. Sci. Eng. **33** (2025) 025007 (16pp) https://doi.org/10.1088/1361-651X/ada784

A non-isothermal phase-field crystal model with lattice expansion: analysis and benchmarks

Maik Punke[1,*], **Marco Salvalaglio**[1,2], **Axel Voigt**[1,2] **and Steven M Wise**[3]

[1] Institute of Scientific Computing, TU Dresden, 01062 Dresden, Germany
[2] Dresden Center for Computational Materials Science, TU Dresden, 01062 Dresden, Germany
[3] Department of Mathematics, The University of Tennessee, Knoxville, TN 37996, United States of America

E-mail: maik.punke@tu-dresden.de

Received 29 August 2024; revised 26 November 2024
Accepted for publication 8 January 2025
Published 22 January 2025

Abstract

We introduce a non-isothermal phase-field crystal model including heat flux and thermal expansion of the crystal lattice. The fundamental thermodynamic relation between internal energy and entropy, as well as entropy production, is derived analytically and further verified by numerical benchmark simulations. Furthermore, we examine how the different model parameters control density and temperature evolution during dendritic solidification through extensive parameter studies. Finally, we extend our framework to the modeling of open systems considering external mass and heat fluxes. This work sets the ground for a comprehensive mesoscale model of non-isothermal solidification including thermal expansion within an entropy-producing framework, and provides a benchmark for further meso- to macroscopic modeling of solidification.

Keywords: solidification, crystal growth, heat flux, phase-field crystal, entropy

---

[*] Author to whom any correspondence should be addressed.

1. Introduction

Solidification of crystalline materials is a ubiquitous phenomenon with wide-ranging implications in both nature and technology. It involves the interaction of different instabilities and out-of-equilibrium growth conditions [1], thus being characterized by competing physical mechanisms and complex morphologies. Managing solidification processes is crucial for conventional technological applications [2, 3] as well as self-assembly approaches [4, 5]. At early stages, crystalline seeds grow either following nucleation or on pre-existing crystal phases/-seeds, while later stages are affected by capillarity, elasticity, plasticity, as well as various kinetic effects [6–10]. Throughout the entire solidification process, heat transfer within the solid and liquid phases significantly impacts the morphology of crystal growth, grain size, and phase distribution [8–11]. On a microscopic level, the arrangement of atoms in a periodic lattice usually results in anisotropic behaviors, such as faceting, and affects the nucleation and movement of defects. These phenomena are closely related to crystallographic directions and are influenced by thermal gradients within the material.

The modeling of solidification has been addressed by various approaches resolving different time- and length-scales of interest. At the scale of individual atoms, microscopic approaches like molecular dynamics techniques [12] describe lattice-dependent features such as anisotropies and defect structures [7]. Due to the limited scaling properties of these models, the growth of crystals, which involves long timescales, is typically not accessible. Macroscopic approaches like sharp-interface and phase-field methods [13–19] coping with large systems and long timescales proved successfully in describing the main features of crystal growth. However, a direct connection to the lattice symmetry and microscopic features is not inherently and self-consistently captured in general and needs to be included through parameters and additional functions, e.g. as anisotropic interface energies [20–22].

The so-called phase-field crystal (PFC) model [23–26] emerged as a prominent approach to describe crystal structures at large (diffusive) timescales through a continuous, periodic order parameter representing the atomic density. It reproduces the main phenomenology for crystalline systems, including solidification and crystal growth, capillarity, lattice deformations as well as nucleation and defect kinematics. The PFC model describes self-consistently anisotropies resulting from the lattice structure [27–29] and inherently includes elasticity effects consistent with continuum mechanics with high accuracy reached when considering dedicated PFC model extensions [30–36]. Therefore, the PFC concept represents a comprehensive framework for the description of crystalline materials in two- and three-dimensions [26, 37, 38].

Only recently, further extensions of the PFC model have been developed to explicitly describe temperature and heat flux phenomena [39–43]. However, thermal expansion or compression of the equilibrium crystal lattice length due to temperature fluctuations is either not considered [39, 40, 43] or entropy production cannot be guaranteed [41, 42]. By further extending the non-isothermal PFC formulations [40, 41], this work presents a non-isothermal PFC model with thermal expansion of the crystal lattice within an entropy-producing framework.

As analytical benchmark, we derive the fundamental thermodynamic relation, describing how the internal energy relates to the entropy, in section 2. We present numerical benchmark simulations in section 3 and examine the role of different model parameters through parameter studies focusing on dendritic solidification, as shown in section 3.1. Finally, we extend our framework to the description of external mass and heat fluxes entering the system via the domain boundary, mimicking the physics of open systems as illustrated in section 3.2. For clarity, the analytical derivation of the entropy production of our model is provided in appendix A.

The analytical results, along with the proposed simulation setups, offer valuable benchmarks for PFC and other solidification modeling approaches that incorporate heat flux in both open and closed systems.

2. Model introduction and analysis

The PFC model [23, 24, 26] describes crystal structures at diffusive timescales through a continuous, periodic order parameter $\psi \equiv \psi(\boldsymbol{x},t)$ representing in its dimensionless formulation the atomic number difference with respect to the liquid phase. It is based on a Swift–Hohenberg-like free energy functional, which can be written

$$F[\psi] = \int_\Omega \left(\frac{\lambda - \kappa}{2}\psi^2 - \delta\frac{\psi^3}{6} + \frac{\psi^4}{12} + \frac{\kappa}{2}\psi\mathcal{L}\psi \right) \mathrm{d}\boldsymbol{x}, \tag{1}$$

with $\delta, \lambda, \kappa \geqslant 0$ parameters characterizing the phase space and material properties together with the global average density $\Psi = \frac{1}{|\Omega|}\int_\Omega \psi\,\mathrm{d}\boldsymbol{x}$, and $\Omega \in \mathbb{R}^n$ the domain of definition of ψ with $n = 2$ defined here as $\Omega = [-L_x/2, L_x/2] \times [-L_y/2, L_y/2]$. The differential operator $\mathcal{L}$ approximates a two-point correlation function and thus encodes the crystal symmetry. For instance, 2D triangular symmetry is obtained as the equilibrium state for some free-energy parameters with $\mathcal{L} = (1+\nabla^2)^2$ [26].

Together with appropriate boundary and initial conditions, the dynamical equation for ψ can be generally described by a conservative gradient flow of F, that is,

$$\partial_t\psi = \nabla \cdot \left(M(\psi)\nabla\frac{\delta F[\psi]}{\delta\psi} \right), \tag{2}$$

where $M(\psi) > 0$ is a mobility function. Further extensions of (1) and (2) may be readily considered to account for other lattice symmetries [44–46] (in both 2D and 3D). In the following, we extend the classical PFC model to a non-isothermal framework that includes thermal lattice expansion and ensures entropy production. The proposed model builds upon previous formulations reported in [40–42]. Extensions are introduced to describe entropy and internal energy densities in a thermodynamically consistent fashion. We remark that such a thermodynamic consistency cannot be guaranteed for the model presented in [41, 42], while no variable lattice parameter (thermal expansion) is considered in [40].

2.1. *Energy and Entropy Densities*

Let T be the dimensionless temperature field with $T = 1$ representing the melting point. It is assumed that the free energy F, entropy S, and internal energy E have the generic forms

$$\begin{aligned} F &= \int_\Omega \hat{f}\left(\psi, \nabla\psi, \nabla^2\psi, T\right) \mathrm{d}\boldsymbol{x}, \\ S &= \int_\Omega \hat{s}\left(\psi, \nabla\psi, \nabla^2\psi, T\right) \mathrm{d}\boldsymbol{x}, \\ E &= \int_\Omega \hat{e}\left(\psi, \nabla\psi, \nabla^2\psi, T\right) \mathrm{d}\boldsymbol{x}. \end{aligned}$$

In [41, 42], we introduced a PFC model with a free energy featuring explicit coupling with the temperature field under periodic boundary conditions for both ψ and T. To derive the entropy and internal energy densities $\hat{s}$ and $\hat{e}$, we propose the following extension of the free energy density $\hat{f}$:

$$\hat{f}\left(\psi,\nabla\psi,\nabla^2\psi,T\right) = f(\psi,T) + \frac{\kappa T}{2}\left(\alpha^2(T)\psi^2 - 2\alpha(T)|\nabla\psi|^2 + \left(\nabla^2\psi\right)^2\right), \tag{3}$$

with

$$f(\psi,T) = k_{\mathrm{B}}T\left(\frac{\lambda-\kappa}{2}\psi^2 - \delta\frac{\psi^3}{6} + \frac{\psi^4}{12}\right) - C_v T\log\left(\frac{T}{T_0}\right) - \beta\psi,$$

where k_{B} is Boltzmann's constant, hereafter set to $k_{\mathrm{B}} \equiv 1$ for simplicity, $C_v > 0$ is the constant heat capacity of the material, $\beta > 0$ is a constant, and $\alpha(T) > 0$ measures the degree of thermal expansion and has physical units (before non-dimensionalization) of length^{-2}. Here, we use the explicit model

$$\alpha(T) = \frac{1}{\left(a_0 + a_1(T - T_0)\right)^2}. \tag{4}$$

$a_0 > 0$ is a reference length (set to $a_0 = 1$), and $a_1 \geqslant 0$ is the thermal expansion coefficient, describing an expansion or compression of the crystal lattice, depending upon whether the temperature T is larger or smaller than the reference temperature, $T_0 > 0$. However, we point out that the theoretical findings presented in this manuscript still hold if a different choice for $\alpha(T)$ is used, since neither the fundamental thermodynamic relation 2.1 nor the entropy production 2.2 depend on the specific choice of $\alpha(T)$. When thermal expansion is neglected ($\alpha \equiv \alpha_0 > 0$), the form of the free energy assumed in [40] is recovered. We use the standard thermodynamic assumptions that

$$\hat{s} = -\partial_T\hat{f} \quad \text{and} \quad \hat{e} = \hat{f} + T\hat{s}. \tag{5}$$

The second condition of (5) encodes a basic assumption of non-equilibrium thermodynamics, namely, that the energy, entropy, and free energy are related locally as if the system were near equilibrium at every point.

As a consequence of (5), we can derive the following fundamental thermodynamic relation describing how the internal energy relates to the entropy:

Proposition 2.1. *Let the free energy density $\hat{f}$, defined as in (3), be a twice continuously differentiable function of temperature, T. Suppose that the entropy and internal energy densities $\hat{s}$ and $\hat{e}$ are computed as in (5). Then,*

$$\frac{1}{T}\frac{\partial\hat{e}}{\partial T} = \frac{\partial\hat{s}}{\partial T}. \tag{6}$$

Proof. Using (5), we have

$$\begin{aligned}\partial_T\hat{e} &= \partial_T\hat{f} + \hat{s} + T\partial_T\hat{s}\\ &= -\hat{s} + \hat{s} + T\partial_T\hat{s}\\ &= T\partial_T\hat{s},\end{aligned}$$

which easily proves the result. □

Using the explicit form of $\hat{f}$ from equations (3), the entropy density $\hat{s}$ and the energy density $\hat{e}$ can be written as

$$\begin{aligned}\hat{s} =& -\partial_T f - \frac{\kappa}{2}\left(\alpha^2(T)\psi^2 - 2\alpha(T)|\nabla\psi|^2 + \left(\nabla^2\psi\right)^2\right)\dots\\ & -\frac{\kappa T}{2}\left(2\alpha(T)\alpha'(T)\psi^2 - 2\alpha'(T)|\nabla\psi|^2\right),\\ \hat{e} =& f - T\partial_T f - \frac{\kappa T^2}{2}\left(2\alpha(T)\alpha'(T)\psi^2 - 2\alpha'(T)|\nabla\psi|^2\right),\end{aligned}$$

leading to

$$\hat{e} = C_v T - \beta\psi - \frac{\kappa T^2}{2}\left(2\alpha(T)\alpha'(T)\psi^2 - 2\alpha'(T)|\nabla\psi|^2\right).$$

In those cases where the thermal expansion may be neglected, that is, $\alpha'(T) \equiv 0$, as in [40], the internal energy density $\hat{e}$ simplifies to

$$\hat{e} = C_v T - \beta\psi.$$

For the general case, we introduce the following definitions:

$$\gamma_0(T) := \kappa T^2\alpha(T)\alpha'(T) \quad \text{and} \quad \gamma_1(T) := \kappa T^2\alpha'(T). \tag{7}$$

The internal energy density can then be expressed as

$$\hat{e} = C_v T - \beta\psi - \gamma_0(T)\psi^2 + \gamma_1(T)|\nabla\psi|^2.$$

2.2. *Mass and internal energy conservation*

We assume that the flow of heat is dominated by diffusive flux. The first law of thermodynamics, which states that energy must be conserved, then takes the form

$$\partial_t\hat{e} = -\nabla\cdot\boldsymbol{J}_e, \tag{8}$$

where $\boldsymbol{J}_e$ is the flux of energy, here chosen as

$$\boldsymbol{J}_e = \widehat{M}_T\nabla\left(\frac{1}{T}\right),$$

where $\widehat{M}_T > 0$ is a thermal energy mobility coefficient so that the energy conservation equation is

$$\begin{aligned}C_v\partial_t T - \beta\partial_t\psi =& -\nabla\left(\widehat{M}_T\nabla\left(\frac{1}{T}\right)\right) + \gamma_0'(T)\psi^2\partial_t T - \gamma_1'(T)|\nabla\psi|^2\partial_t T\\ & + 2\gamma_0(T)\psi\,\partial_t\psi - 2\gamma_1(T)\nabla\psi\cdot\nabla\partial_t\psi.\end{aligned} \tag{9}$$

Based on the general form of the energy equation, it follows directly that the first law of thermodynamics holds globally, $\partial_t E = 0$.

The generic form of the mass conservation equation is

$$\partial_t\psi = -\nabla\cdot\boldsymbol{J}_\psi,$$

with mass flux $\boldsymbol{J}_\psi$, imposing $\partial_t\int_\Omega\psi(\boldsymbol{x},t)\,\mathrm{d}\boldsymbol{x} = 0$. For $\boldsymbol{J}_\psi$, we assume $\boldsymbol{J}_\psi = -M_\psi\nabla w$ with mass mobility coefficient $M_\psi > 0$ and generalized chemical potential w:

$$\partial_t\psi = \nabla\cdot\left(M_\psi\nabla w\right), \qquad \text{(mass conservation)} \tag{10}$$

$$w = \partial_\psi \left(\frac{\hat{f}}{T}\right) - \nabla \cdot \left(\partial_{\nabla\psi}\left(\frac{\hat{f}}{T}\right)\right) + \kappa\nabla^4\psi, \qquad \text{(generalized chemical potential).} \tag{11}$$

We observe that

$$\frac{\hat{f}}{T} = \widetilde{f}(\psi) - C_v \log\left(\frac{T}{T_0}\right) - \beta\frac{\psi}{T} + \frac{\kappa}{2}\left(\alpha^2(T)\psi^2 - 2\alpha(T)|\nabla\psi|^2 + \left(\nabla^2\psi\right)^2\right),$$

where

$$\widetilde{f}(\psi) := \frac{\lambda-\kappa}{2}\psi^2 - \delta\frac{\psi^3}{6} + \frac{\psi^4}{12},$$

and, therefore, the generalized chemical potential w can be specified as

$$\begin{aligned} w &= \partial_\psi\left(\frac{\hat{f}}{T}\right)\partial_t\psi - \nabla\cdot\left(\partial_{\nabla\psi}\left(\frac{\hat{f}}{T}\right)\right) + \nabla^2\left(\partial_{\nabla^2\psi}\left(\frac{\hat{f}}{T}\right)\right) \\ &= \widetilde{f}'(\psi) - \frac{\beta}{T} + \kappa\alpha^2(T)\psi + 2\kappa\nabla\cdot(\alpha(T)\nabla\psi) + \kappa\nabla^4\psi. \end{aligned}$$

Proposition 2.2. *Assume that* Ω *is a rectangular domain in* $\mathbb{R}^2$ *and the fields are* Ω*-periodic. With the flux choices for* $\boldsymbol{J}_\mathrm{e}$ *and* $\boldsymbol{J}_\psi$ *above, the entropy is increasing in time, with the following entropy-production rate:*

$$\partial_t S = \int_\Omega \left\{ M_\psi |\nabla w|^2 + \hat{M}_T\left|\nabla\left(\frac{1}{T}\right)\right|^2\right\} \mathrm{d}\boldsymbol{x} \geqslant 0. \tag{12}$$

The explicit demonstration is given in appendix A.

2.3. PFC model recapitulation

As stated earlier, we use periodic boundary conditions for simplicity. We assume a constant mass mobility coefficient $M_\psi > 0$, and we suppose that the thermal energy mobility coefficient satisfies $\widehat{M}_T = T^2 M_T$, where $M_T > 0$ is a constant. The complete model results in a coupled system of equations that includes a heat-like equation and a PFC-like equation:

$$\begin{aligned} M_T\nabla^2 T &= \left(C_v - \gamma_0'(T)\psi^2 + \gamma_1'(T)|\nabla\psi|^2\right)\partial_t T - \left(\beta + 2\gamma_0(T)\psi - 2\gamma_1(T)\nabla\psi\cdot\nabla\right)\partial_t\psi, \\ \partial_t\psi &= M_\psi\nabla^2\left((\lambda-\kappa)\psi - \delta\frac{\psi^2}{2} + \frac{\psi^3}{3} - \frac{\beta}{T} + \kappa\alpha^2(T)\psi + 2\kappa\nabla\cdot(\alpha(T)\nabla\psi) + \kappa\nabla^4\psi\right) \end{aligned} \tag{13}$$

where $\gamma_0(T)$ and $\gamma_1(T)$ defined as in equation (7) and $\alpha(T)$ as in equation (4). In addition to those parameters that are essential for the standard isothermal PFC model, namely, the parameters $\delta, \lambda, \kappa \geqslant 0$ and the global average density Ψ, our proposed non-isothermal model (13) includes mobility constants $M_\psi, M_T > 0$, the material constant $\beta > 0$ controlling the coupling of the PFC equation with the heat flux, the heat capacity $C_v > 0$ and a thermal expansion coefficient $a_1 \geqslant 0$ which enters $\alpha(T)$, encoding how the crystal lattice expands due to temperature fluctuations. We will investigate in the following section 3.1 how the individual model parameters affect crystal growth within closed systems and extend our formulations to the modeling

Table 1. Model parameters for all the simulations reported in this paper. We set $\lambda = 0.6$, $\kappa = 0.46$, and $\delta = 1$. For the setup according to figures 1–3 the domain is set to $\Omega = 220 \times 256\text{UC}$, while for the setup according to figure 4, we choose $\Omega = 441 \times 128\text{UC}$ with 1 unit cell (UC) representing the smallest repeat unit of ψ: $1\text{UC} = [0, p_x] \times [0, p_y]$ and $p_x = 2/\sqrt{3}p_y = 4\pi/\sqrt{3}$. Uniform spatial and temporal grids are chosen to guarantee numerical convergence and entropy production. Consistent with the established PFC literature utilizing the Fourier pseudo-spectral method, see e.g. [24, 47, 48], we choose for all simulations $\Delta x \approx \Delta y \approx 1$ with $\Delta t = 0.01$ for the setup according to figures 1–3 and $\Delta t = 0.1$ for the setup according to figure 4. Empty table entries read as the row above.

Figure	Ψ	C_v	M_T	M_ψ	β	a_1	T_0
1	0.849,0.151	0.06	0.06	1	0.06	0.1	0.6
2		$0.05\ldots 2$					
		0.06	$2 \cdot 10^{-3}\ldots 0.3$				
			0.06	$0.01\ldots 100$			
3				1	$6 \cdot 10^{-4}\ldots 0.3$		
					0.06	$0.01\ldots 0.3$	
						0.1	$0.1\ldots 1.8$
4	—					0.01	0.6

of open systems in section 3.2. Table 1 summarizes all model parameters for the simulations reported in this paper. Here, we consider growth regimes where the solid phase is favored close to solid-liquid coexistence. Similar to classical PFC approaches, other regimes, such as the stripe phase with its associated coexistence with the triangular phase, are accessible in the corresponding phase diagram, although their extensive discussion is beyond the scope of the present work.

3. Numerical benchmark simulations

Numerical solutions of the proposed model can be obtained efficiently by using a Fourier pseudo-spectral method, enforcing periodic boundary conditions in combination with a linear first-order semi-implicit (IMEX) time-stepping scheme. The numerical algorithm is implemented on graphics process units (GPUs), and we perform the (inverse-) Fourier transforms using a cuFFT library.

3.1. Model features and parameter studies

We focus on a benchmark setup of a growing crystal in a supersaturated melt with initially constant temperature T_0 to investigate the density and temperature evolution in a closed system for different model parameter values, similar to [41]. We choose our model- and material parameters as reported in table 1 and compare the resulting density and temperature evolution for the global average densities $\Psi = \Psi_0 (= 0.849)$ and $\Psi = 1 - \Psi_0 (= 0.151)$ in figure 1, representing crystals with underlying honeycomb and triangular symmetry, respectively. For the chosen values of Ψ, the melt is mass-supersaturated, enabling solidification of the growing crystal within a closed system. Representative steps of the dendritic solidification process are shown in figure 1(a) with snapshots of the density and temperature fields. Relative to the commonly observed enlarged lattice spacing produced by PFC models during growth [41, 49], further compression of the crystal lattice is obtained for heat reduction inside the solid

(a) density and temperature evolution

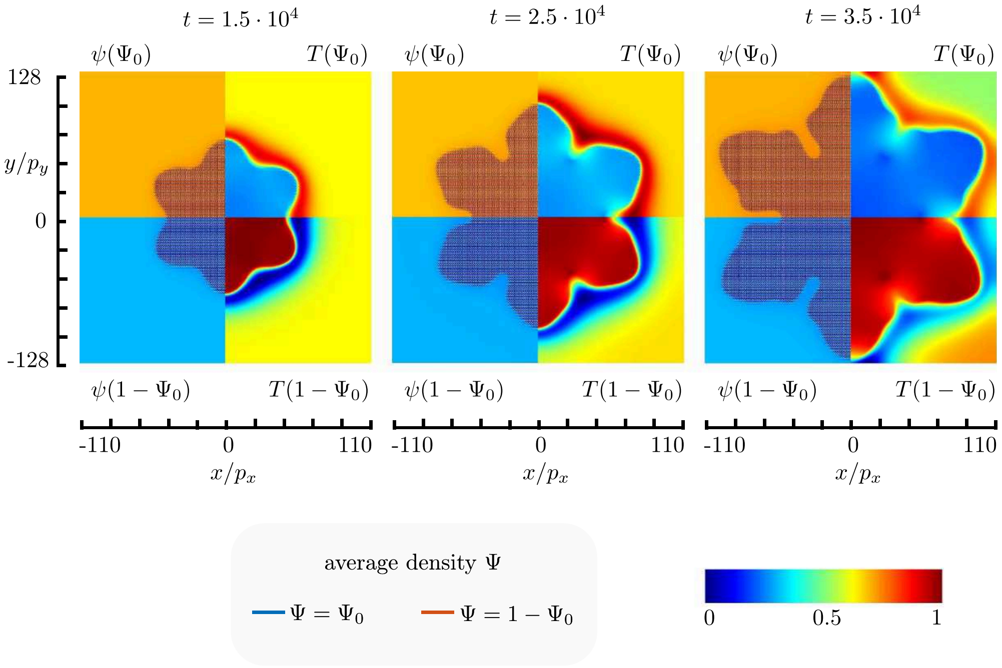

(b) area of the solid phase

(c) temperature difference

(d) entropy-production rate

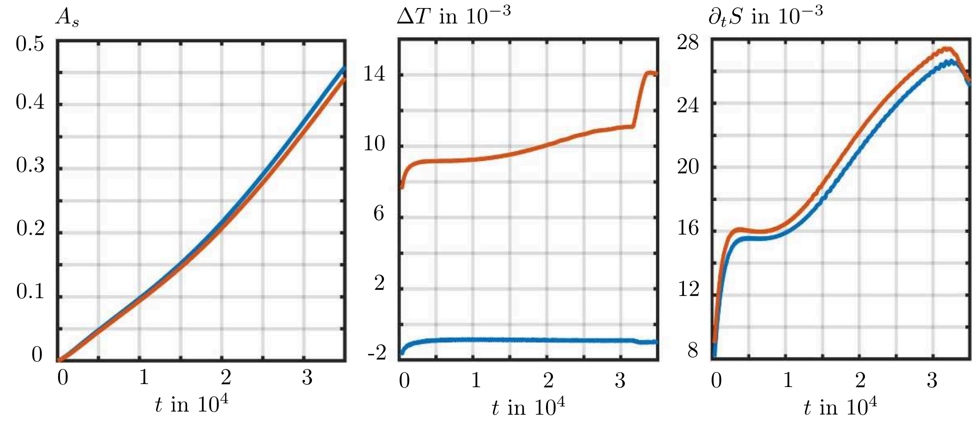

Figure 1. Dendritic solidification by the proposed PFC model. The symmetry break for average densities $\Psi = \Psi_0$ and $\Psi = 1 - \Psi_0$ during dendritic solidification is also illustrated. (a) Density (ψ) and temperature (T) evolution for $\Psi = \Psi_0$ (top) and $\Psi = 1 - \Psi_0$ (bottom) during growth at different time steps. (b) Relative area of the solid phase A_s vs. time (c) signed temperature difference ΔT vs. time. (d) Entropy-production rate $\partial_t S$ vs. time. For illustration purposes, we normalized the plotted quantities $\psi(\Psi_0)$, $\psi(1-\Psi_0)$ and $T(1-\Psi_0)$ from 0 to 1 and normalized the plotted quantity $T(\Psi_0)$ from 0 to 0.9 in order to ensure a consistent color representation for $T = T_0$ across all plots. Values of $\psi(\Psi_0)$, $\psi(1-\Psi_0)$, $T(\Psi_0)$ and $T(1-\Psi_0)$ vary within the following ranges: $-0.03 \leqslant \psi(\Psi_0) \leqslant 1.21$, $-0.02 \leqslant \psi(1-\Psi_0) \leqslant 0.97$, $0.6 - 6 \cdot 10^{-4} \leqslant T(\Psi_0) \leqslant 0.6 + 6 \cdot 10^{-4}$ and $0.6 - 1.0 \cdot 10^{-2} \leqslant T(1-\Psi_0) \leqslant 0.6 + 3.6 \cdot 10^{-3}$. Lengths are scaled with the atomic spacings along the x- and y-axis, p_x and p_y.

phase ($\Psi = \Psi_0$) and a further expansion of the crystal lattice is obtained for heat production inside the solid phase ($\Psi = 1 - \Psi_0$), as described by equation (4). Next to a qualitatively different temperature evolution inside the solid phase for $\Psi = \Psi_0$ and $\Psi = 1 - \Psi_0$, an additional (small) symmetry break in the dendritic morphologies is observed (slightly faster solidification dynamics corresponding to smaller temperature gradients for $\Psi = \Psi_0$, further analysis below). As first described in [41], only in case $a_1 = 0$, identical energetics for $\Psi = \Psi_0$ and $\Psi = 1 - \Psi_0$ lead to identical density and temperature morphologies. To further inspect this symmetry break, we quantify the dendritic growth process by calculating the relative area of the solid phase A_s (area of the solid phase divided by the domain size) and show its time evolution in figure 1(b), illustrating a slightly faster growth of the solid phase for $\Psi = \Psi_0$. Additionally, we calculate the signed temperature difference within the system as $\Delta T(t) = |\max_{\boldsymbol{x}\in\Omega} T(\boldsymbol{x},t) - \min_{\boldsymbol{x}\in\Omega} T(\boldsymbol{x},t)|\,\mathrm{sign}\,(T(\boldsymbol{x}=0,t) - T_0)$, leading to positive values for a solidification process with heat development inside the solid phase (e.g. for $\Psi = 1 - \Psi_0$) and to negative values for a solidification process with heat reduction inside the solid phase (e.g. for $\Psi = \Psi_0$). In figure 1(c), we show the time evolution of ΔT and observe a larger temperature difference within the system for $\Psi = 1 - \Psi_0$, corresponding to slower solidification dynamics. The different energetics for $\Psi = \Psi_0$ and $\Psi = 1 - \Psi$ lead to different entropy-production rates $\partial_t S$ (2.2), which we show in figure 1(d). We note that after the initial transient behavior for $t \lesssim 2 \cdot 10^3$, the entropy-production rates for $\Psi = \Psi_0$ and $\Psi = 1 - \Psi_0$ remain unchanged until they increase for $t \gtrsim 1 \cdot 10^4$ due to the developing dendritic arms. The interaction of the density and temperature fields with their periodic images leads to a decrease in $\partial_t S$ for $t \gtrsim 3.1 \cdot 10^4$, see figure 1(d).

We further investigate the role of different parameters entering the proposed PFC model, equation (13), during the dendritic solidification process for $\Psi = \Psi_0$ and $\Psi = 1 - \Psi_0$ through numerical parameter studies. We vary one of the following parameters while letting the others unchanged: M_ψ, M_T, C_v, a_1, β and T_0, see table 1. We keep the setup from figure 1, calculate A_s, ΔT at $t = 3.5 \cdot 10^4$ for both $\Psi = \Psi_0$ and $\Psi = 1 - \Psi_0$ and show their dependence on the different model parameters in figures 2 and 3.

For larger parameter values of M_ψ, M_T and lower parameter values of C_v, an increase in A_s is obtained, corresponding to a faster solidification of the growing dendrites, see figure 2(a). The temperature field inside the growing solid phase can be controlled quantitatively by varying M_ψ, M_T, and C_v, but does not change its qualitative behavior (heat production inside the solid phase for $\Psi = 1 - \Psi_0$ and heat reduction inside the solid phase for $\Psi = \Psi_0$), see figure 2(b). We conclude that M_ψ, M_T, and C_v mainly control the time scales of our model.

By varying the parameter values of a_1, β, and T_0, the relative area of the growing solid phase A_s shows a maximum for $\Psi = \Psi_0$ and $\Psi = 1 - \Psi_0$, respectively, see figure 3(a). The maximal values of A_s correspond to parameter values a_1, β and T_0 which lead to vanishing temperature differences ($\Delta T \approx 0$), see figure 3(b). Furthermore, a changed qualitative behavior of the temperature field inside the growing solid phase is obtained for large parameter values of a_1, T_0, and small parameter values of β (heat reduction inside the solid phase for $\Psi = 1 - \Psi_0$ and heat production inside the solid phase for $\Psi = \Psi_0$), see figure 3(b). This qualitative change in the temperature fields corresponds to a flipped sign of the prefactor for $\partial_t \psi$ within the heat-like equation (13) for large parameter values of a_1, T_0 and small parameter values of β.

We numerically verified that entropy production is obtained for all simulations in figures 1–3.

(a) area of the solid phase

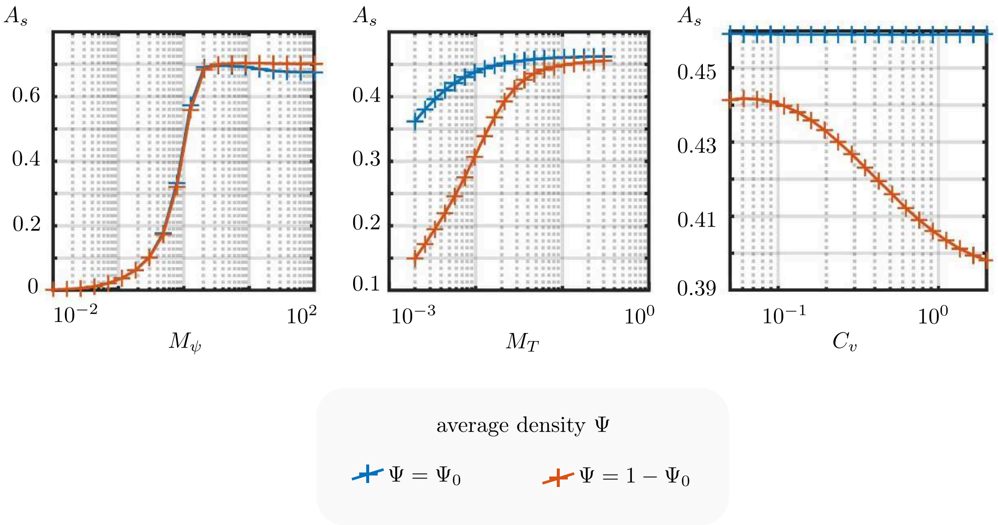

(b) temperature difference

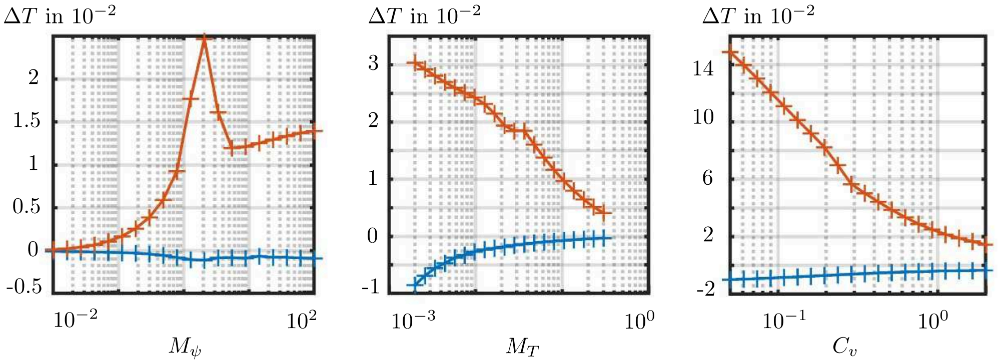

Figure 2. Dependence on model parameters—I. The mobility parameters M_ψ, M_T and C_v mainly control the dynamics of the solidification process for the setup in figure 1: (a) area of the solid phase A_s and (b) temperature difference ΔT, by varying M_ψ, M_T and C_v.

3.2. Open systems

To properly describe solidification in open systems, we need to modify our model to mimic external mass and heat fluxes entering the system via the domain boundary. We will show that the modified model (described below) recovers qualitative behavior typical of the directionality of mass fluxes as well as (de-)stabilization effects of the growth front induced by heat fluxes during solidification, thus describing more realistic solidification conditions than the supersaturation condition typically used for closed systems, see section 3.1.

We initialize a perturbed crystal front surrounded by liquid with $\psi \equiv 0.87$ for $|x| < 33p_x$, see figure 4(a), and material parameters from table 1. The specific choice of the material parameters guarantees a local equilibrium of the solid and liquid crystal phase for $|x| < 33p_x$. For $|x| > 193p_x$ we initialize a liquid crystal phase with lower density $\psi \equiv 0.86$. For $33p_x \leqslant |x| \leqslant 193p_x$ the density of the liquid crystal phase decreases linearly from $\psi\,|_{|x|=33p_x} =$

(a) area of the solid phase

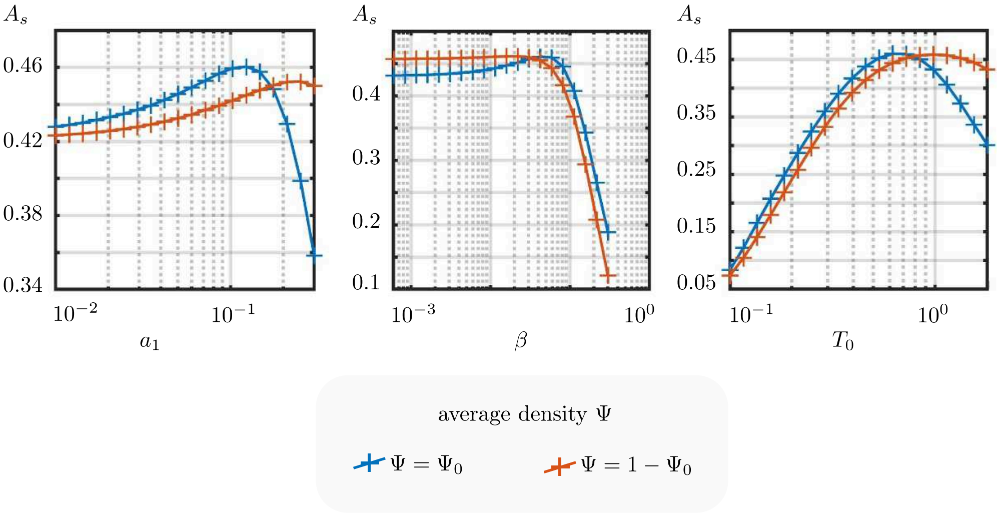

(b) temperature difference

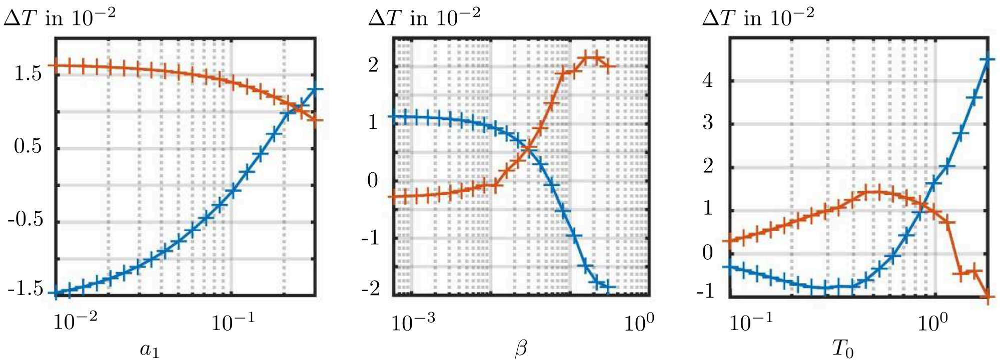

Figure 3. Dependence on model parameters—II. The material parameters a_1, β and T_0 control the dynamics of the solidification process and the qualitative behavior of the associated temperature field for the setup in figure 1: (a) area of the solid phase A_s and (b) temperature difference ΔT, by varying a_1, β and T_0.

0.87 to $\psi|_{|x|=193p_x} = 0.86$. At every time step, we adjust the density for $|x| \geqslant 193p_x$ setting $\psi|_{|x|\geqslant 193p_x} = 0.86$, thus effectively introducing a net mass flux into the system. This adjustment directs mass towards the central crystal front, analogous to liquid diffusion observed in experimental setups [3, 11, 50]. Since the solid and liquid crystal phases in the central region are initialized in equilibrium, the additional mass flux leads to an incipient solidification at the central crystal front.

Furthermore, the stability of the growing crystal front is expected to depend on the presence (and sign) of temperature gradients, see e.g. [51]. To test the capabilities of the approach, we therefore consider nonuniform temperatures and explore regimes featuring opposite temperature gradients. Like the density initialization described above, we set $T|_{|x|<33p_x} \equiv T_0$ and

(a) initial density field

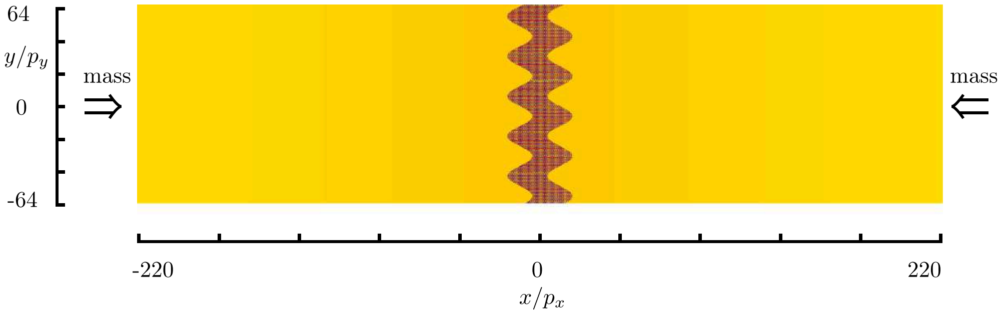

(b1) initial temperature field
heat reduction applied

(b2) initial temperature field
heat increase applied

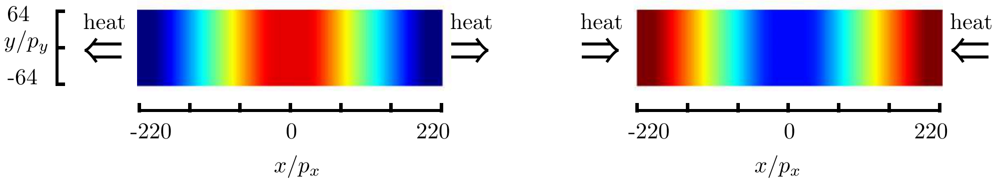

(c1) density field at $t = 1.5 \cdot 10^5$
heat reduction applied

(c2) density field at $t = 2 \cdot 10^6$
heat increase applied

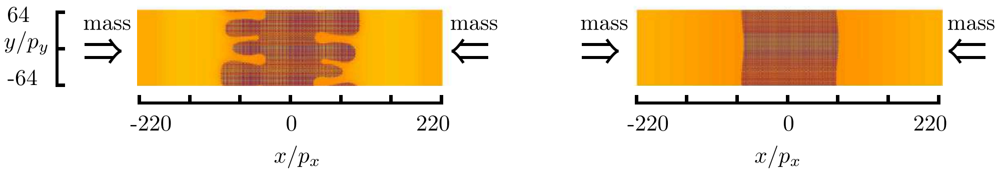

Figure 4. Example of growth in an open system and interplay with the heat flux. (a) Initial condition corresponding to a perturbed crystal morphology. Mass flux entering the system, inducing crystallization, is considered. (b1) Initial temperature field enforcing heat reduction, leading to a dendritic-like solid-liquid interface evolution shown in (c1) by the microscopic density at $t = 1.5 \cdot 10^5$. (b2) Initial temperature field enforcing heat increase, leading to a smooth growing front shown in (c2) by the microscopic density at $t = 2 \cdot 10^6$. For illustration purposes, we normalized all plotted quantities from 0 to 1 using the color-scale from figure 1, values of ψ and T vary within the following ranges: (a) $0.41 \leqslant \psi \leqslant 1.09$, (b1) $0.25 \leqslant T \leqslant 0.6$, (c1) $0.02 \leqslant \psi \leqslant 1.21$, (b2) $0.6 \leqslant T \leqslant 0.95$, (c2) $0.03 \leqslant \psi \leqslant 1.21$. Lengths are scaled with the atomic spacings along the x- and y-axis, p_x and p_y.

adjust the temperature for $|x| > 193p_x$ setting $T|_{|x| \geqslant 193p_x} \equiv T_b$ at every time step. In case the applied temperature gradient is set opposite to the growth direction of the solid phase ($T_0 > T_b = 0.25$), a destabilization of the evolving solid-liquid interface leading to dendritic solidification is observed, see figures 4(b1) and (c1). When enforcing a temperature gradient along the growth direction ($T_0 < T_b = 0.95$), a stabilization of the initially perturbed solid-liquid interface is obtained, leading to a smoother growth front and slower solidification dynamics, see figures 4(b2) and (c2). This result is consistent with theoretical [52–55] and, importantly, experimental observations [51, 56–59].

4. Conclusion

We introduced a non-isothermal PFC model that accounts for lattice expansion ensuring entropy production for time evolutions. Thermodynamic consistency is shown to follow by construction from the chosen formulation of the free energy as well as heat and mass fluxes. Through numerical benchmark simulations, we showcase how the parameters entering the model control temperature and density evolution during dendritic solidification processes and further verify entropy production numerically. Finally, we extend our model formulation to include the description of external mass and heat fluxes that enter the system, thus mimicking the physics of open systems. This work not only extends the existing non-isothermal PFC formulations [40, 41] but also allows for thermodynamic consistent PFC simulations of realistic solidification conditions incorporating thermal expansion of the crystal lattice and including heat fluxes.

Our model phenomenologically introduces the simplest free-energy formulation that ensures entropy production, making it a valuable benchmark for future non-isothermal frameworks. For instance, an alternative approach, building on the classical density functional theory of freezing, could involve incorporating a temperature-dependent lattice parameter within the energy formulations of [39, 43] and deriving the resulting governing equations under the condition of entropy production.

The proposed numerical simulations offer accessible benchmarks for PFC and other solidification modeling and simulation approaches. The extension to three-dimensional systems can be envisaged with the aid of efficient numerical methods [38, 60] or coarse-grained formulations of the PFC, like the so-called amplitude expansion of the PFC model [61–63]. Additionally, explicitly modeling elastic relaxation can provide a better description of competitive time scales, particularly regarding elastic relaxation and diffusive dynamics [30, 32, 33], along with the presence of heat flux.

Data availability statement

The data that support the findings of this study are openly available at the following URL/DOI: https://doi.org/10.5281/zenodo.13270551.

Acknowledgments

M P and M S acknowledge support from the Emmy Noether Programme of the Deutsche Forschungsgemeinschaft (DFG, German Research Foundation)—Project No. 447241406. A V and M S acknowledge support from the Deutsche Forschungsgemeinschaft (DFG, German Research Foundation) within FOR3013—Project No. 417223351. S M W gratefully acknowledges support from the US National Science Foundation under Grant NSF-DMS 2309547. Computing resources have been provided by the Center for Information Services and High-Performance Computing (ZIH), the NHR Center of TU Dresden.

Appendix A. Entropy production

We explicitly demonstrate that in the proposed model, the entropy is increasing in time. By taking the time derivative of the total entropy and using equations (6) and (8), we have

$$\begin{aligned}
\partial_t S &= \int_\Omega \left\{ \partial_\psi \hat{s}\, \partial_t \psi + \partial_T \hat{s}\, \partial_t T + \partial_{\nabla\psi} \hat{s} \cdot \partial_t \nabla\psi + \partial_{\nabla^2\psi} \hat{s}\, \partial_t \left(\nabla^2 \psi\right) \right\} \mathrm{d}\boldsymbol{x} \\
&= \int_\Omega \left\{ \partial_\psi \hat{s}\, \partial_t \psi + \frac{1}{T} \partial_T \hat{e}\, \partial_t T + \partial_{\nabla\psi} \hat{s} \cdot \nabla \partial_t \psi + \partial_{\nabla^2\psi} \hat{s}\, \nabla^2 \partial_t \psi \right\} \mathrm{d}\boldsymbol{x} \\
&= \int_\Omega \left\{ \partial_\psi \hat{s}\, \partial_t \psi + \partial_{\nabla\psi} \hat{s} \cdot \nabla \partial_t \psi + \partial_{\nabla^2\psi} \hat{s}\, \nabla^2 \partial_t \psi \right\} \mathrm{d}\boldsymbol{x} \ldots \\
&\quad + \int_\Omega \left\{ \frac{1}{T} \left(-\nabla \cdot \boldsymbol{J}_e - \partial_\psi \hat{e}\, \partial_t \psi - \partial_{\nabla\psi} \hat{e} \cdot \nabla \partial_t \psi - \partial_{\nabla^2\psi} \hat{e}\, \nabla^2 \partial_t \psi \right) \right\} \mathrm{d}\boldsymbol{x} \\
&= -\int_\Omega \left\{ \partial_\psi \left(\frac{\hat{f}}{T} \right) \partial_t \psi + \partial_{\nabla\psi} \left(\frac{\hat{f}}{T} \right) \cdot \nabla \partial_t \psi + \partial_{\nabla^2\psi} \left(\frac{\hat{f}}{T} \right) \nabla^2 \partial_t \psi + \frac{1}{T} \nabla \cdot \boldsymbol{J}_e \right\} \mathrm{d}\boldsymbol{x}.
\end{aligned}$$

Using periodic boundary conditions, integration-by-parts, and mass conservation, we have

$$\begin{aligned}
\partial_t S &= \int_\Omega \left\{ -\left(\partial_\psi \left(\frac{\hat{f}}{T} \right) \partial_t \psi - \nabla \cdot \left(\partial_{\nabla\psi} \left(\frac{\hat{f}}{T} \right) \right) + \nabla^2 \left(\partial_{\nabla^2\psi} \left(\frac{\hat{f}}{T} \right) \right) \right) \partial_t \psi - \frac{1}{T} \nabla \cdot \boldsymbol{J}_e \right\} \mathrm{d}\boldsymbol{x} \\
&= \int_\Omega \left\{ w \nabla \cdot \boldsymbol{J}_\psi - \frac{1}{T} \nabla \cdot \boldsymbol{J}_e \right\} \mathrm{d}\boldsymbol{x} \\
&= \int_\Omega \left\{ -\nabla w \cdot \boldsymbol{J}_\psi + \nabla \left(\frac{1}{T} \right) \cdot \boldsymbol{J}_e \right\} \mathrm{d}\boldsymbol{x}.
\end{aligned}$$

Finally, using the flux conditions that appear in equations (9)–(11), namely

$$\boldsymbol{J}_\psi = -M_\psi \nabla w \quad \text{and} \quad \boldsymbol{J}_e = \widehat{M}_T \nabla \left(\frac{1}{T} \right),$$

we obtain

$$\partial_t S = \int_\Omega \left\{ M_\psi \left| \nabla w \right|^2 + \hat{M}_T \left| \nabla \left(\frac{1}{T} \right) \right|^2 \right\} \mathrm{d}\boldsymbol{x} \geqslant 0.$$

Appendix B. Stable parameter ranges

For the setup illustrated in figure 1, we examined the range of parameters where our model remains numerically stable. Similar to figure 2 and 3, we set $C_v = 0.06$, $M_T = 0.06$, $M_\psi = 1$, $\beta = 0.06$, $a_1 = 0.1$, $T_0 = 0.6$ and varied one parameter while letting the others unchanged. For $\Psi = \Psi_0$, we observed numerical convergence of our model for the following parameter ranges:

$$\begin{aligned}
0.02 \lesssim C_v &< \infty \\
0 < M_T &\lesssim 0.8 \\
10^{-3} \lesssim M_\psi &< \infty \\
0 < \beta &\lesssim 0.51 \\
0 < a_1 &\lesssim 0.34 \\
0.1 \lesssim T_0 &\lesssim 1.86.
\end{aligned} \tag{B.1}$$

For $\Psi = 1 - \Psi_0$, within the following parameter ranges numerical convergence of our model was found:

$$\begin{aligned} 0.03 \lesssim C_v &< \infty \\ 0 < M_T &\lesssim 0.5 \\ 10^{-3} \lesssim M_\psi &< \infty \\ 0 < \beta &\lesssim 0.41 \\ 0 < a_1 &\lesssim 0.31 \\ 0.09 \lesssim T_0 &\lesssim 1.93. \end{aligned} \tag{B.2}$$

ORCID iDs

Maik Punke https://orcid.org/0000-0002-3564-7942
Marco Salvalaglio https://orcid.org/0000-0002-4217-0951
Axel Voigt https://orcid.org/0000-0003-2564-3697
Steven M Wise https://orcid.org/0000-0003-3824-2075

References

[1] Langer J S 1980 *Rev. Mod. Phys.* **52** 1–28
[2] Flemings M C 1974 *Metall. Mater. Trans.* B **5** 2121–34
[3] Dantzig J A and Rappaz M 2016 *Solidification: Revised & Expanded* (EPFL Press) (available at: www.epflpress.org/product/501/9782889142071/solidification)
[4] Stangl J, Holý V and Bauer G 2004 *Rev. Mod. Phys.* **76** 725–83
[5] Polshettiwar V, Baruwati B and Varma R S 2009 *ACS Nano* **3** 728–36
[6] Boettinger W, Coriell S, Greer A, Karma A, Kurz W, Rappaz M and Trivedi R 2000 *Acta Mater.* **48** 43–70
[7] Hoyt J J, Asta M and Karma A 2003 *Mater. Sci. Eng.* R **41** 121–63
[8] Jaafar M A, Rousse D R, Gibout S and Bédécarrats J P 2017 *Renew. Sust. Energ. Rev.* **74** 1064–79
[9] Gránásy L, Tóth G I, Warren J A, Podmaniczky F, Tegze G, Rátkai L and Pusztai T 2019 *Prog. Mater. Sci.* **106** 100569
[10] Alexandrov D V and Galenko P K 2021 *Philos. Trans. R. Soc.* A **379** 20200325
[11] Chalmers B 1964 *Principles of Solidification* (*Applied Solid State Physics*) (Springer) pp 161–70
[12] Alder B J and Wainwright T E 1959 *J. Chem. Phys.* **31** 459–66
[13] Kobayashi R 1993 *Physica* D **63** 410–23
[14] Karma A and Rappel W J 1998 *Phys. Rev.* E **57** 4323–49
[15] Zhu M and Stefanescu D 2007 *Acta Mater.* **55** 1741–55
[16] Steinbach I 2009 *Model. Simul. Mater. Sci. Eng.* **17** 073001
[17] Pan S and Zhu M 2010 *Acta Mater.* **58** 340–52
[18] Takaki T 2014 *ISIJ Int.* **54** 437–44
[19] Kaiser J, Adami S, Akhatov I and Adams N 2020 *Int. J. Heat Mass Transfer* **155** 119800
[20] Suzuki T, Ode M, Kim S G and Kim W T 2002 *J. Cryst. Growth* **237–239** 125–31
[21] Torabi S, Lowengrub J, Voigt A and Wise S 2009 *Proc. R. Soc.* A **465** 1337–59
[22] Salvalaglio M, Backofen R, Bergamaschini R, Montalenti F and Voigt A 2015 *Cryst. Growth Des.* **15** 2787–94
[23] Elder K R, Katakowski M, Haataja M and Grant M 2002 *Phys. Rev. Lett.* **88** 245701
[24] Elder K R and Grant M 2004 *Phys. Rev.* E **70** 051605
[25] Provatas N and Elder K 2010 *Phase-Field Methods in Materials Science and Engineering* (Wiley) (https://doi.org/10.1002/9783527631520)
[26] Emmerich H, Löwen H, Wittkowski R, Gruhn T, Tóth G I, Tegze G and Gránásy L 2012 *Adv. Phys.* **61** 665–743
[27] Backofen R and Voigt A 2009 *J. Phys.: Condens. Matter* **21** 464109
[28] Podmaniczky F, Tóth G I, Pusztai T and Gránásy L 2014 *J. Cryst. Growth* **385** 148–53

[29] Ofori-Opoku N, Warren J A and Voorhees P W 2018 *Phys. Rev. Mater.* **2** 083404
[30] Skogvoll V, Salvalaglio M and Angheluta L 2022 *Modelling Simul. Mater. Sci. Eng.* **30** 084002
[31] Heinonen V, Achim C V, Elder K R, Buyukdagli S and Ala-Nissila T 2014 *Phys. Rev.* E **89** 032411
[32] Heinonen V, Achim C V, Kosterlitz J M, Ying S C, Lowengrub J and Ala-Nissila T 2016 *Phys. Rev. Lett.* **116** 024303
[33] Skaugen A, Angheluta L and Viñals J 2018 *Phys. Rev. Lett.* **121** 255501
[34] Skaugen A, Angheluta L and Viñals J 2018 *Phys. Rev.* B **97** 054113
[35] Salvalaglio M, Voigt A and Elder K R 2019 *npj Comput. Mater.* **5** 48
[36] Salvalaglio M, Chockalingam K, Voigt A and Dörfler W 2022 *Ex. Counterexamples* **2** 100067
[37] Tegze G, Tóth G I and Gránásy L 2011 *Phys. Rev. Lett.* **106** 195502
[38] Tang S, Backofen R, Wang J, Zhou Y, Voigt A and Yu Y M 2011 *J. Cryst. Growth* **334** 146–52
[39] Kocher G and Provatas N 2019 *Phys. Rev. Mater.* **3** 053804
[40] Wang C and Wise S M 2022 *J. Math. Study* **55** 337–57
[41] Punke M, Wise S M, Voigt A and Salvalaglio M 2022 *Modelling Simul. Mater. Sci. Eng.* **30** 074004
[42] Punke M, Wise S M, Voigt A and Salvalaglio M 2023 *Proc. Appl. Math. Mech.* **23** e202200112
[43] Burns D, Provatas N and Grant M 2024 *Acta Mater.* **267** 119712
[44] Greenwood M, Provatas N and Rottler J 2010 *Phys. Rev. Lett.* **105** 045702
[45] Greenwood M, Rottler J and Provatas N 2011 *Phys. Rev.* E **83** 031601
[46] Mkhonta S K, Elder K R and Huang Z F 2013 *Phys. Rev. Lett.* **111** 035501
[47] Cheng M and Warren J A 2008 *J. Comput. Phys.* **227** 6241–8
[48] Tegze G, Bansel G, Tóth G I, Pusztai T, Fan Z and Gránásy L 2009 *J. Comput. Phys.* **228** 1612–23
[49] Punke M, Skogvoll V and Salvalaglio M 2023 *Proc. Appl. Math. Mech.* **23** e202300213
[50] Cole G 1971 *Metall. Trans.* **2** 357–70
[51] Losert W, Shi B and Cummins H 1998 *Proc. Natl Acad. Sci.* **95** 431–8
[52] Du L and Zhang R 2014 *Integr. Mater. Manuf. Innov.* **3** 225–39
[53] Tang J and Xue X 2009 *J. Mater. Sci.* **44** 745–53
[54] Kim S G and Kim W T 2001 *Mater. Sci. Eng.* A **304** 281–6
[55] Fu L, Cao Y, Gao Z, Dong L and Du L 2020 *Eur. Phys. J.* E **43** 1–6
[56] Chang J, Wang H, Zhou K and Wei B 2012 *Appl. Phys.* A **109** 139–43
[57] Cao C, Wang F, Duan L and Bai X 2011 *Sci. China Phys. Mech. Astron.* **54** 89–94
[58] Song R, Dai F and Wei B 2011 *Sci. China Phys. Mech. Astron.* **54** 901–8
[59] Yang X, Fujiwara K, Maeda K, Nozawa J, Koizumi H and Uda S 2011 *Appl. Phys. Lett.* **98** 012113
[60] Yamanaka A, McReynolds K and Voorhees P W 2017 *Acta Mater.* **133** 160–71
[61] Goldenfeld N, Athreya B P and Dantzig J A 2005 *Phys. Rev.* E **72** 020601
[62] Athreya B P, Goldenfeld N and Dantzig J A 2006 *Phys. Rev.* E **74** 011601
[63] Salvalaglio M and Elder K R 2022 *Modelling Simul. Mater. Sci. Eng.* **30** 053001